JOURNAL OF PROPULSION AND POWER
Vol. 19, No. 2, March–April 2003

Proper Orthogonal Decomposition of Turbine Rotor–Stator Interaction

Paul G. A. Cizmas*
Texas A&M University, College Station, Texas 77843-3141
and
Antonio Palacios†
San Diego State University, San Diego, California 92182-7720

Numerical simulations of the flow in a one-stage turbine are carried out to investigate the feasibility of constructing a reduced-order model via Galerkin methods. The flow in the turbine is modeled by the unsteady Reynolds-averaged Navier–Stokes equations. The governing equations are written in the strong conservation form and solved using a fully implicit, finite difference approximation. By the use of the proper orthogonal decomposition (POD), spatial dominant features, also known as POD modes or eigenfunctions, are identified and separated from the spatiotemporal dynamics of the turbine flow. The POD reconstructed solutions indicate that a significant portion of the original dynamics is captured by a few modes. The solution reconstructed using the first 40 modes captures more than 99% of the energy spectrum, whereas the error of the energy variable is less than 0.6%, and the error of skin friction is less than 1.5%. Phase-space plots further indicate the existence of low-dimensional dynamics, which supports the validity of a reduced-order model for turbine flow.

Nomenclature

a	=	speed of sound
$\hat{c}$	=	chord length
e	=	total energy per unit volume
(F, G)	=	inviscid flux vectors in curvilinear coordinates
(f, g)	=	inviscid flux vectors in Cartesian coordinates
h	=	enthalpy
J	=	Jacobian of transformation from curvilinear curvilinear to Cartesian coordinates
Pr	=	Prandtl number
p	=	static pressure
$\boldsymbol{Q}$	=	vector of unknowns in curvilinear coordinates
$\boldsymbol{q}$	=	vector of unknowns in Cartesian coordinates
q	=	heat flux vector
Re	=	Reynolds number, $Re = \hat{\rho}_\infty \hat{a}_\infty \hat{c}/\hat{\mu}_\infty$
T	=	temperature or period
t	=	time in Cartesian coordinates
(u, v)	=	components of velocity vector
(x, y)	=	Cartesian coordinates
γ	=	ratio of specific heats
ϵ	=	error measure
μ	=	viscosity
(ξ, η)	=	curvilinear coordinates
ρ	=	fluid density
τ	=	time in curvilinear coordinates, shear stress tensor, or nondimensional skin friction
Φ	=	basis function

Subscripts

FM	=	full-model solution
POD	=	POD reconstruction solution
t	=	time derivative
x	=	derivative with respect to x
y	=	derivative with respect to y
∞	=	upstream infinity

Superscripts

$\hat{}$	=	dimensional
$*$	=	thin-layer, stagnation value or complex conjugate

Received 29 April 2002; revision received 2 November 2002; accepted for publication 7 November 2002.

*Assistant Professor, Department of Aerospace Engineering. Associate Fellow AIAA.
†Assistant Professor, Department of Mathematics.

Introduction

THE continuous improvement of computer hardware has allowed engineers and scientists to simulate complex phenomena numerically using more realistic models. Examples of numerical simulations of complex flows include weather prediction, multistage turbomachinery flow, and multiphase flow reactors. The governing equations describing these phenomena consist of a system of highly coupled partial differential equations. Solving these equations is a difficult and computing intensive task. For example, the flow simulation of a three-row turbine with the simplest blade count of 1:1:1 exceeded 21 days on a Cray C90 supercomputer.[1]

Modeling the flow physics in the rotor–stator interaction is important for designing high-efficiency, reliable compressors and turbines. Potential flow interaction, wake interaction, hot streak interaction, vortex shedding, and blade flutter are the most important phenomena present in the rotor–stator interaction. The interaction between these phenomena makes the simulation challenging and requires a large computational effort. In addition, the large number of geometric and flow parameters makes it expensive to include the numerical simulation of rotor–stator interactions in the turbomachinery design system.

One solution for reducing the high turnaround time and the associated cost of such a numerical simulation is parallel computation using the more cost-effective massively parallel processing platforms. The first parallel algorithms developed for unsteady flows in turbomachinery were reported by Eulitz et al.[2] and Cizmas and Subramanya.[3] The much shorter turnaround time has allowed significant progress in the investigation of turbomachinery flows.[4–6] In spite of a reduction in the total turnaround time through parallel processing, the total computational time has not been modified.

Another way to reduce the high turnaround time of unsteady flow simulations is to develop reduced-order models of the fluid flow.

Until recently, there has been no attempt to use reduction-order techniques in fluid dynamics applications, although these techniques have been common practice in structural dynamics for years. In one of the first attempts, the eigenfrequencies of the fluid flow about an isolated airfoil modeled with a Navier–Stokes computational fluid dynamics algorithm were used to better understand the influence of artificial viscosity on numerical stability.[7,8] Subsequently, several eigenmode-based reduced-order aerodynamics models were developed in the frequency domain for airfoils, wings, and cascades using vortex lattice models or linearized unsteady potential flows.[9–11] Reduced-order models of unsteady viscous flow in turbomachinery were also developed in the frequency domain.[12,13] A reduced-order model in the time domain was developed for isolated airfoils, based on an explicit Euler solver.[14]

The common feature of these reduced-order models is that they were developed for small perturbations about a nonlinear steady flowfield. Unfortunately, the small perturbation assumption is an important limiting factor, and, as a result, the reduced-order models based on the eigenfunctions of the linearized flow are not appropriate for flows with large time perturbations. A reduced-order model, however, can be developed for complex flows with large time and spatial perturbations using the proper orthogonal decomposition method. Recent investigations have proved the applicability of a reduced-order model based on proper orthogonal decomposition to a transonic aeroelastic panel that experiences oscillatory motions of a normal shock.[15]

The objective of this paper is to demonstrate the feasibility of constructing a reduced-order model using the Galerkin method for rotor–stator interaction in turbomachinery flows. The next section describes the governing equations and the numerical method used to simulate the turbine flow. The proper orthogonal decomposition and its numerical implementation are presented in the following section. Numerical results for a one-stage turbine are subsequently presented.

Flow Model

The first part of this section presents the governing equations that model the rotor–stator interaction in turbomachinery. The second part describes the numerical method used to solve the governing equations. This part also presents the grid generation, the boundary conditions implementation, and the parallel computation paradigm.

Governing Equations

The unsteady compressible flow through a multistage axial compressor or turbine with arbitrary blade counts is modeled using the Reynolds-averaged Navier–Stokes equations. The flow is modeled as quasi three dimensional. The computational domain associated with each airfoil is divided into an inner region, near the airfoil, and an outer region, away from the airfoil. The flow is assumed to be fully turbulent. The eddy viscosity is computed using the Baldwin–Lomax model and the kinematic viscosity is computed using Sutherland's law.

To simulate flows of arbitrary geometries, the governing equations are discretized using body-fitted curvilinear coordinates (ξ, η, τ) as opposed to using the Cartesian coordinates (x, y, t). The governing equations are nondimensionalized using freestream quantities:

$$(x, y) = (\hat{x}, \hat{y})/\hat{c}, \qquad (u, v) = (\hat{u}, \hat{v})\Big/\sqrt{\hat{p}_\infty/\hat{\rho}_\infty}, \qquad \rho = \hat{\rho}/\hat{\rho}_\infty$$

$$p = \hat{p}/\hat{p}_\infty, \qquad T = \gamma(\hat{T}/\hat{T}_\infty), \qquad e = \hat{e}/\hat{p}_\infty, \qquad \mu = \hat{\mu}/\hat{\mu}_\infty$$

$$h = \hat{h}(\hat{p}_\infty/\hat{\rho}_\infty), \qquad q = \hat{q}\Big/\left(\hat{p}_\infty\sqrt{\hat{p}_\infty/\hat{\rho}_\infty}\right)$$

The thin-layer Navier–Stokes equations, written in vectorial form, are

$$\frac{\mathrm{d}\boldsymbol{Q}}{\mathrm{d}\tau} + \frac{\mathrm{d}\boldsymbol{F}}{\mathrm{d}\xi} + \frac{\mathrm{d}\boldsymbol{G}}{\mathrm{d}\eta} = \frac{\sqrt{\gamma}M_\infty}{Re}\frac{\mathrm{d}\boldsymbol{S}^*}{\mathrm{d}\eta} \tag{1}$$

where

$$\boldsymbol{Q} = \boldsymbol{q}/J, \qquad \boldsymbol{F} = (\xi_t\boldsymbol{q} + \xi_x\boldsymbol{f} + \xi_y\boldsymbol{g})/J$$

$$\boldsymbol{G} = (\eta_t\boldsymbol{q} + \eta_x\boldsymbol{f} + \eta_y\boldsymbol{g})/J$$

The Jacobian of the coordinate transformation is $J = \xi_x\eta_y - \eta_x\xi_y$, $\boldsymbol{q}$ is the state vector, and $\boldsymbol{f}$ and $\boldsymbol{g}$ are the flux vectors in Cartesian coordinates

$$\boldsymbol{q} = \begin{bmatrix} \rho \\ \rho u \\ \rho v \\ e \end{bmatrix}, \qquad \boldsymbol{f} = \begin{bmatrix} \rho u \\ \rho u^2 + p \\ \rho uv \\ (e+p)u \end{bmatrix}, \qquad \boldsymbol{g} = \begin{bmatrix} \rho v \\ \rho uv \\ \rho v^2 + p \\ (e+p)v \end{bmatrix} \tag{2}$$

The vector $\boldsymbol{S}^*$ contains the viscous stresses

$$\boldsymbol{S}^* = \frac{1}{J}\begin{bmatrix} 0 \\ K_1u_\eta + K_2\eta_x \\ K_1v_\eta + K_2\eta_y \\ K_1\left\{Pr^{-1}(\gamma-1)^{-1}(a^2)_\eta + [(u^2+v^2)/2]_\eta\right\} \\ \quad + K_2(u\eta_x + v\eta_y) \end{bmatrix} \tag{3}$$

where

$$K_1 = \mu\left(\eta_x^2 + \eta_y^2\right), \qquad K_2 = \mu(\eta_x u_\eta + \eta_y v_\eta)/3$$

Numerical Method

This section briefly describes the numerical model and the method used for solving the governing equations. Further details can be found in a paper by Cizmas and Dorney.[4] The Navier–Stokes equations are written in the strong conservative form. The fully implicit, finite difference approximation is solved iteratively at each time level, using an approximate factorization method. Two Newton–Raphson subiterations are used to reduce the linearization and factorization errors at each time step. The convective terms are evaluated using a third-order accurate upwind-biased Roe scheme, and the viscous terms are evaluated using second-order accurate central differences. The scheme is second-order accurate in time.

Grid Generation

Two types of grids are used to discretize the flowfield surrounding the rotating and stationary grids.[3,16] An O grid is used to resolve the Navier–Stokes equations near the airfoil, where the viscous effects are important. An H grid is used to discretize the governing equations away from the airfoil. The O grid is generated using an elliptical method. The H grid is algebraically generated. The O and H grids are overlaid. The flow variables are communicated between the O and H grids through bilinear interpolation. The H grids corresponding to consecutive rotors and stators are allowed to slip past each other to simulate the relative motion.

Boundary Conditions

Because multiple grids are used to discretize the Navier–Stokes equations, two classes of boundary conditions must be enforced on the grid boundaries, namely, natural boundary conditions and zonal boundary conditions. The natural boundaries include inlet, outlet, periodic, and the airfoil surfaces. The zonal boundaries include the patched and overlaid boundaries.

The inlet boundary conditions include the specification of flow angle, average total pressure, and downstream propagating Riemann invariant. The upstream propagating Riemann invariant is extrapolated from the interior of the domain. At the outlet, the average static pressure is specified, whereas the downstream propagating Riemann invariant, circumferential velocity, and entropy are extrapolated from the interior of the domain. Periodicity is enforced by matching flow conditions between the lower surface of the lowest H grid of a row and the upper surface of the topmost H grid of

the same row. At the airfoil surface, the following boundary conditions are enforced: no slip, adiabatic wall, and zero normal pressure gradient.

For the zonal boundary conditions of the overlaid boundaries, data are transferred from the H grid to the O grid along the O grid's outermost grid line. Data are then transferred back to the H grid along its inner boundary. At the end of each iteration, an explicit, corrective, interpolation procedure is performed. The patch boundaries are treated similarly, using linear interpolation to update data between adjoining grids.[16]

Parallel Computation

The parallel code uses message-passing interface libraries and runs on various parallel computers, from Beowulf-type personal computer clusters to massively parallel processors such as the Cray T3E. One processor is allocated for the O and H grids corresponding to each airfoil. One processor is allocated for each inlet and outlet H grid. Interprocessor communication is used to match boundary conditions between grids. Periodic boundary conditions are imposed by cyclic communication patterns within rows. Interblade-row boundary conditions are imposed by gather-send_receive-broadcast communication routines between adjacent rows. Load imbalance issues need to be considered at grid generation time to reduce synchronization overhead.[17]

Proper Orthogonal Decomposition

The proper orthogonal decomposition (POD) is a well-known technique for determining an optimal basis for the reconstruction of a data set.[18,19] The POD has been used in various disciplines that include fluid mechanics,[20–22] identification and control in chemical engineering,[23] oceanography,[24] image processing,[25] and flutter prediction.[26] Depending on the discipline, the POD is also known as Karhunen–Loève decomposition, principal components analysis, singular systems analysis, and singular value decomposition. This section reviews the definitions and properties of the POD relevant to this work and discusses how the method can be applied to computer simulations to separate spatial and temporal behavior.

Theoretical Aspects

Consider a sequence of numerical and/or experimental observations represented by scalar functions $u(\boldsymbol{x}, t_i)$, $i = 1, \ldots, M$. These functions are assumed to be a linear infinite dimensional Hilbert space L^2 on a domain D that is a bounded subset of $\mathbb{R}^n$, and they are parametrized by t_i, which represents time. The (time) average of the sequence, defined by

$$\bar{u}(\boldsymbol{x}) = \langle u(\boldsymbol{x}, t_i) \rangle = \frac{1}{M} \sum_{i=1}^{M} u(\boldsymbol{x}, t_i) \tag{4}$$

is assumed to be zero, without loss of generality. The POD extracts time-independent orthonormal basis functions $\Phi_k(\boldsymbol{x})$ and time-dependent orthonormal amplitude coefficients $a_k(t_i)$, such that the reconstruction

$$u(\boldsymbol{x}, t_i) = \sum_{k=1}^{M} a_k(t_i)\, \Phi_k(\boldsymbol{x}), \qquad i = 1, \ldots, M \tag{5}$$

is optimal in the sense that the average least-square truncation error

$$\varepsilon_m = \left\langle \left\| u(\boldsymbol{x}, t_i) - \sum_{k=1}^{m} a_k(t_i) \Phi_k(\boldsymbol{x}) \right\|^2 \right\rangle \tag{6}$$

is a minimum for any given number $m \leq M$ of basis functions over all possible sets of orthogonal functions. Here $\| \ \|$ is the L^2-norm $\| f \|^2 = (f, f)$, where the symbols in parentheses denote the standard Euclidean inner product. The functions $\Phi_k(\boldsymbol{x})$ are called empirical eigenfunctions, coherent structures, or POD modes. They are computed as follows. First, the optimality property (6) is equivalent to finding functions Φ that maximize the normalized average projection of u onto Φ

$$\max_{\Phi \in L^2(D)} \frac{\langle |(u, \Phi)|^2 \rangle}{\| \Phi \|^2} \tag{7}$$

where $| \ |$ denotes the modulus. Then, it can be shown[20] that the optimum condition (7) reduces to the eigenvalue problem

$$\int_D \langle u(\boldsymbol{x}) u^*(\boldsymbol{y}) \rangle \Phi(\boldsymbol{y})\, \mathrm{d}\boldsymbol{y} = \lambda \Phi(\boldsymbol{x}) \tag{8}$$

where $\boldsymbol{x}, \boldsymbol{y} \in D$. It follows that the optimal basis functions $\{\Phi_k\}$ are the eigenfunctions of the integral equation (8), whose kernel is the averaged autocorrelation function

$$\langle u(\boldsymbol{x}) u^*(\boldsymbol{y}) \rangle \equiv R(\boldsymbol{x}, \boldsymbol{y})$$

In practice, the state of a numerical model is only available at discrete spatial grid points, so that the observations that form the data set are vectors rather than continuous functions. In other words, $D = (x_1, x_2, \ldots, x_N)$, where x_j is the jth grid point and $u(\boldsymbol{x}, t_i)$ is the vector $\boldsymbol{u}_i = [u(x_1, t_i), u(x_2, t_i), \ldots, u(x_N, t_i)]^T$. The data set can be obtained from numerical simulation, experimental investigation, or a combination of the numerical and experimental results. In the discrete case, the autocorrelation function is replaced by the tensor product matrix

$$R(\boldsymbol{x}, \boldsymbol{y}) = \frac{1}{M} \sum_{i=1}^{M} u(\boldsymbol{x}, t_i) u^T(\boldsymbol{y}, t_i) \tag{9}$$

More importantly, it can also be shown that the eigenvectors of the $R(\boldsymbol{x}, \boldsymbol{y})$ matrix yield the eigenfunctions $\Phi_k(\boldsymbol{x})$, which can be computed with the algorithm presented in the following section.

Computational Implementation: Method of Snapshots

A popular technique for finding the eigenvectors of Eq. (9) is the method of snapshots developed by Sirovich.[27] It was introduced as an efficient method when the resolution of the spatial domain N is higher than the number of observations M. The method of snapshots is based on the data vectors $\boldsymbol{u}_i$ and the eigenvectors $\boldsymbol{\Phi}_k$ spanning the same linear space.[21,27] This implies that the eigenvectors can be written as a linear combination of the data vectors

$$\boldsymbol{\Phi}_k = \sum_{i=1}^{M} v_i^k \boldsymbol{u}_i, \qquad k = 1, \ldots, M \tag{10}$$

After substitution in the eigenvalue problem, $R(\boldsymbol{x}, \boldsymbol{y}) \Phi(\boldsymbol{y}) = \lambda \Phi(\boldsymbol{x})$, the coefficients v_i^k are obtained from the solution of

$$C \boldsymbol{v} = \lambda \boldsymbol{v} \tag{11}$$

where $\boldsymbol{v^k} = (v_1^k, \ldots, v_M^k)$ is the kth eigenvector of Eq. (11), and C is a symmetric $M \times M$ matrix defined by $[c_{ij}] = (1/M)(\boldsymbol{u}_i, \boldsymbol{u}_j)$. Here the symbols in parentheses denote the standard vector inner product, $(\boldsymbol{u}_i, \boldsymbol{u}_j) = u(x_1, t_i) u(x_1, t_j) + \cdots + u(x_N, t_i) u(x_N, t_j)$. In this way, the eigenvectors of the $N \times N$ matrix R [Eq. (9)] can be found by computing the eigenvectors of an $M \times M$ matrix C [Eq. (11)], a preferable task if $N \gg M$. The results presented in the following section were obtained with an implementation of the method of snapshots. An iterative quadratic regulator method[28] was used to compute the eigenvectors of the symmetric matrix C, [Eq. (11)].

Results

This section presents the results obtained by applying the POD method to the flow simulation in a one-stage turbine. The analysis is focused on the POD of the energy variable e. Results are also presented for density and skin-friction coefficient.

Turbine Description

The turbine used for the numerical simulation had 32 stator airfoils and 48 rotor airfoils. The radius at midspan was approximately 1 m. The solidity of the stator row was 0.93 and the solidity of the rotor row was 0.91. The flow conditions for the test turbine are given in Table 1. The flow in the turbine is subsonic.

To reduce the computational effort to only one interblade passage per row, it was assumed that there were an equal number of blades in each turbine row. As a result, the rotor airfoils were rescaled by a 48/32 factor. An investigation of the influence of airfoil count on the turbine flow showed that the unsteady effects were amplified when a simplified airfoil count 1:1 was used.[29] Consequently, the results obtained using the simplified airfoil count represent an upper limit for the unsteady effects.

Accuracy of Numerical Results

To validate the accuracy of the numerical results, it was necessary to show that the results were independent of the grid that discretizes the computational domain. Three grids were used to assess the solution grid independence. The coarse grid had 35 grid points normal to the airfoil and 150 grid points along the airfoil in the O grid, and 50 grid points in the axial direction and 50 grid points in the circumferential direction in the H grid. The stator airfoil and rotor airfoil had the same number of grid points. The number of grid points of the other two grids is shown in Table 2.

The coarse grid is presented in Fig. 1, where, for clarity, every other grid point in each direction is shown. The distance between the grid points on the airfoil and the next layer of grid points around the airfoil was the same for the coarse, medium, and fine grids to have the same y^+ number. The grid was generated such that, for the given flow conditions, the y^+ number was less than 1. Approximately 20 grid points were used to discretize the boundary layers.

The results presented in this paper were computed using two Newton subiterations per time step and 3000 time steps per cycle. Here, a cycle is defined as the time required for a rotor to travel a distance equal to the pitch length at midspan. To ensure time periodicity, each simulation was run in excess of 80 cycles, although usually between 20 and 40 cycles are sufficient for a solution started from scratch.

The flow in the rotor row included the influences of the upwind stator row. As a result, if there were differences between the results due to different grid sizes, these differences would be the largest in the rotor row. For this reason the rotor row was used to assess the grid independence of the numerical results. The nondimensional skin friction, $\tau = \mu(\mathrm{d}u/\mathrm{d}y)/[\mu_\infty(u_\infty/c)]$, was used to validate the grid solution independence.

Before the grid independence of the numerical results is validated, the periodicity of the unsteady solution must be verified. Solution periodicity was assessed by comparing the results of consecutive cycles. Figure 2 shows the maximum-, averaged-, and minimum-over-cycle values of skin friction for three consecutive cycles. Because

Table 1 Turbine flow conditions

Quantity	Units	Value
Inlet Mach number M_{inlet}	——	0.155
Reynolds number Re	——	65799
Inlet temperature T_{inlet}	K	1860
Pressure ratio $p_{\text{exit}}/p^*_{\text{inlet}}$	——	0.68
Rotational speed n	rotations/min	3600

Table 2 Grid points for the single-stage turbine

Location	Coarse grid	Medium grid	Fine grid
H-grid inlet	24×50	36×75	54×112
H-grid airfoil, stator	50×50	75×75	112×112
O-grid airfoil, stator	150×35	225×53	337×79
H-grid airfoil, rotor	50×50	75×75	112×112
O-grid airfoil, rotor	150×35	225×53	337×79
H-grid outlet	24×50	36×75	54×112
Total grid points	17,900	40,500	90,430

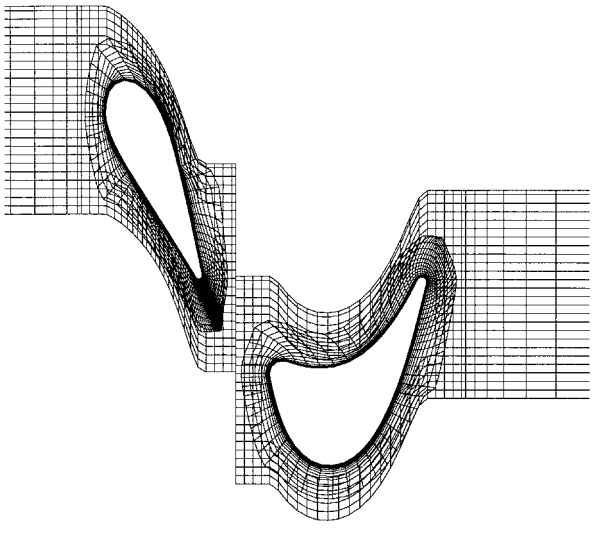

Fig. 1 Coarse grid (every other point in each direction shown).

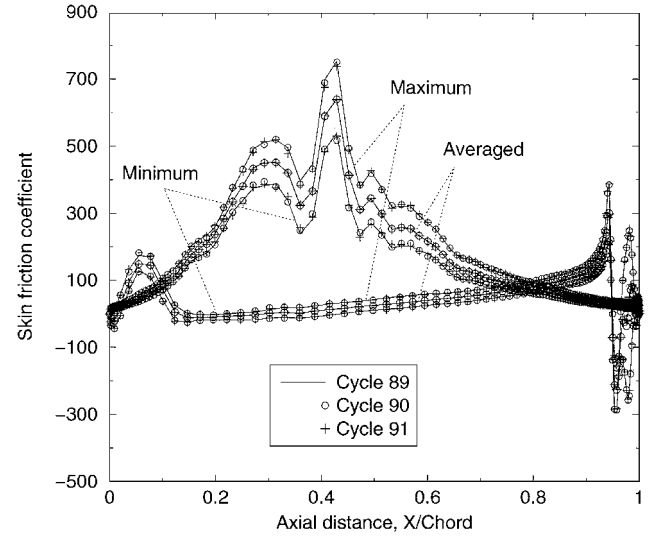

Fig. 2 Maximum-, averaged-, and minimum-over-cycle skin friction at three consecutive cycles.

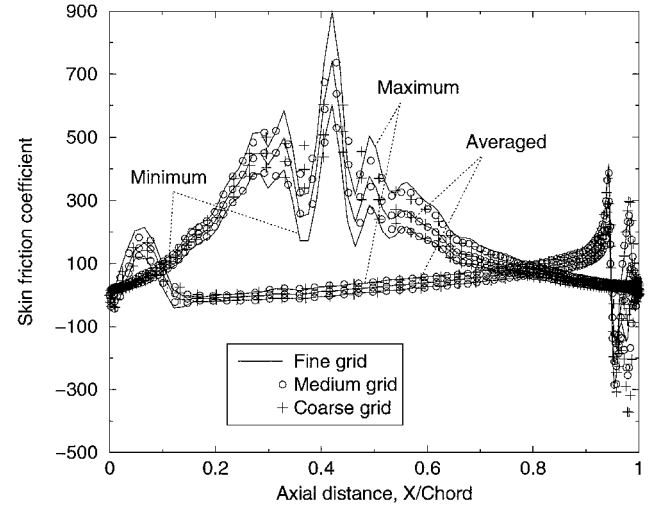

Fig. 3 Maximum-, averaged-, and minimum-over-cycle skin friction for coarse, medium, and fine grids.

the values of the skin friction were almost identical for the three consecutive cycles, the solution was considered periodic.

To validate the grid independence, three values of the skin friction were compared: the averaged, minimum, and maximum over one cycle. The comparison of the skin-friction coefficients computed using the three grids is shown in Fig. 3. The largest difference between the skin friction on the coarse and fine grids was 29.8%. This maximum difference was located near the trailing edge, on the suction side. The average difference between the coarse grid skin friction and the fine grid skin friction was 2.4%. Good agreement was obtained between the results corresponding to the medium and fine grid, the average difference being 0.8%. As a result, the numerical results were grid independent only for the medium and fine grids. The medium grid was used for the computation of all subsequent results presented in this paper.

POD of Energy

The numerical simulation developed herein uses the conservative state vector $\boldsymbol{q} = \{\rho, \rho u, \rho v, e\}^T$. The spatiotemporal variation of the four variables, ρ, ρu, ρv, and e is quite different. The energy e varies the most, whereas the density ρ varies the least. Consequently, the POD of energy is the most challenging. As a result, if one can prove that energy variation is properly captured by the POD, then one can be confident that the variation of the other variables could also be captured. Note that the energy e, which is a state variable, is different from the relative energy E_k. The relative energy captured by the kth mode, E_k, is defined by

$$E_k = \lambda_k \Big/ \sum_{j=1}^{M} \lambda_j \tag{12}$$

where $\lambda_1 \geq \lambda_2, \ldots, \geq \lambda_k \geq, \ldots, \geq 0$. Note that the cumulative sum of relative energies,

$$\sum E_{k\,\mathrm{sc}}$$

approaches one as the number of modes in the reconstruction increases.

The spatiotemporal variation of energy e in the stator is shown in Fig. 4. The nondimensional energy varies between approximately 2.25 and 3.41. The time-averaged energy shown in Fig. 5 varies from 2.27 to 3.39. For the POD a snapshot of the solution was saved every 10 time steps, whereas the blade passing period was divided into 3000 time steps. Consequently, 300 snapshots were saved over a blade passing period. The variation of the first and third POD modes is approximately the same, from approximately −0.04 to 0.016. The second and fourth modes vary from −0.065 to 0.075.

A similar result is obtained for the rotor. The energy varies between 1.99 and 3.02, whereas the time-averaged energy varies between 2.10 and 2.94. As shown in Fig. 6, the first and second POD modes of the energy vary between −0.02 and 0.02. The third and forth energy modes vary from −0.07 to 0.05.

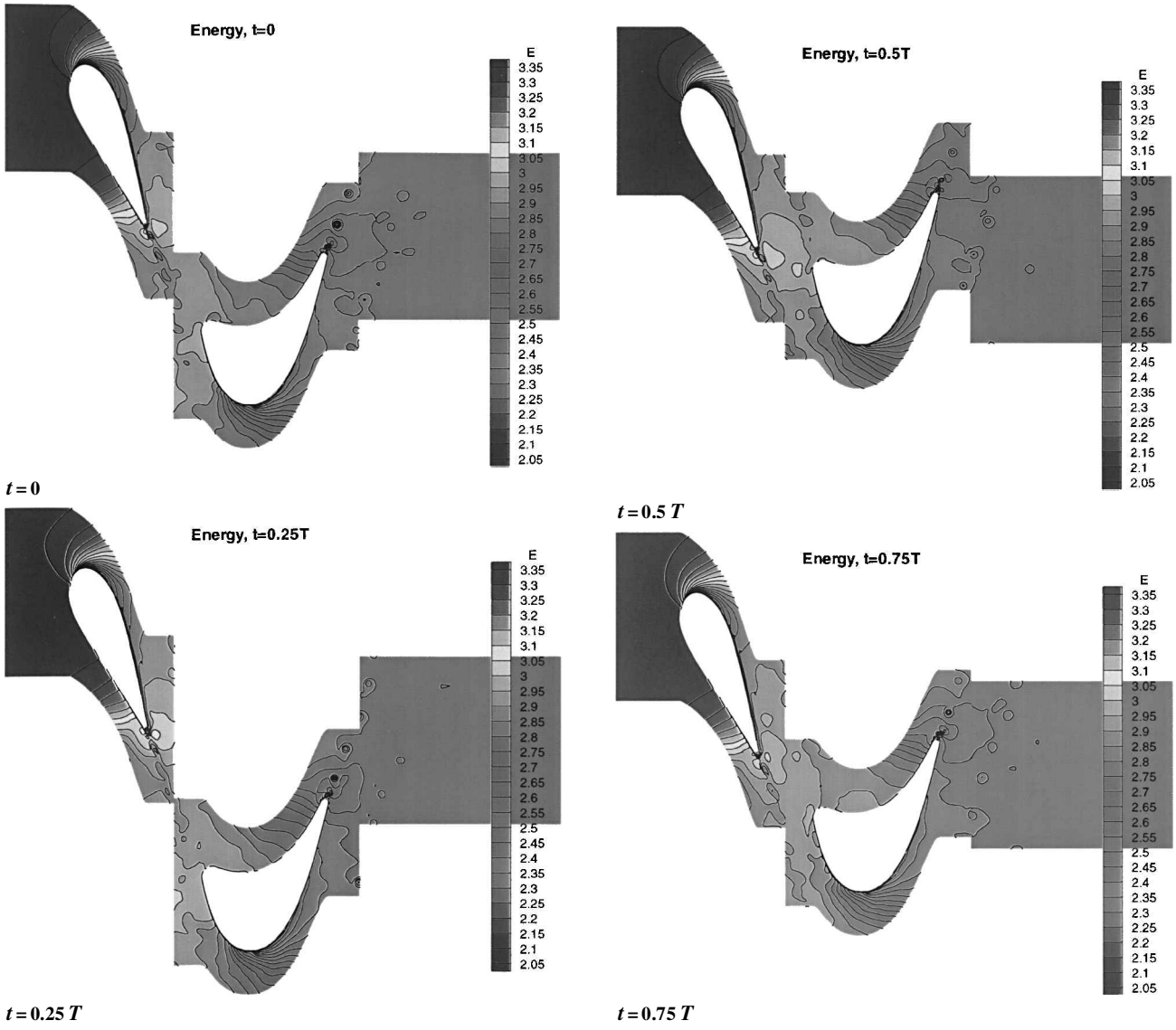

Fig. 4 Spatiotemporal variations of state variable e recorded at equal time intervals during one period T of the flow motion.

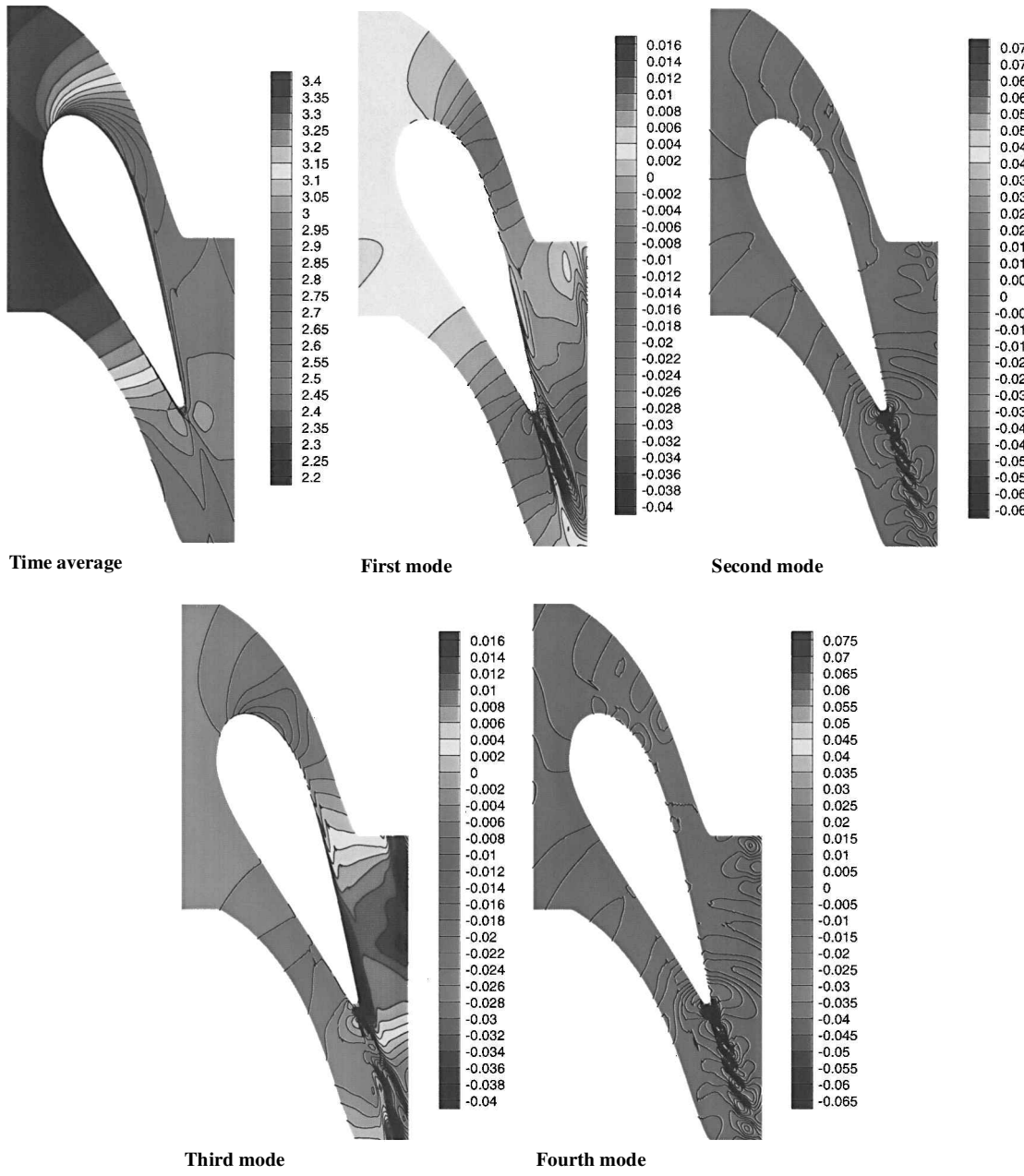

Fig. 5 Five most relevant POD modes for the state variable e on the stator airfoil.

Note that for both the stator and the rotor, the variation of the first POD mode of energy e is smaller than that of higher POD modes. As shown in Fig. 7a, for both the stator and the rotor, the relative energy of the first mode is approximately 30%, whereas the relative energy of the second mode is approximately 20%. The relative energy of the fifth mode is under 3% for both rows. As shown in Fig. 7b, over 80% of the energy is contained in the first four modes. The first 20 modes capture 95.4% of the energy, whereas the first 40 modes capture 99.4%.

The temporal coefficients $a_k(t)$ are calculated here in by projecting the data set on each of the eigenfunctions

$$a_k(t) = [u(\boldsymbol{x}, t), \Phi_k(\boldsymbol{x})], \qquad i = 1, \ldots, M \qquad (13)$$

The first four temporal coefficients $a_k(t)$, associated with the four most energetic POD modes, are shown in Fig. 8. Note that on the ordinate, the rotor scale is twice the stator scale. For both Figs. 8a and 8b, notice two different timescales. The first timescale is equal to the period of the passing blade. The second timescale is about one order of magnitude smaller than the first timescale. For the stator, the first and the third temporal coefficients have the same period, equal to the period of the passing blade. The second and fourth temporal coefficients have a period equal to approximately one-tenth of the period of the passing blade. For the rotor, the first and the second temporal coefficients have the same period, equal to the period of the passing blade. The third and fourth temporal coefficients have a period equal to approximately one-seventh of the period of the passing blade.

Phase-space projections of the POD amplitude coefficients of energy e are shown in Fig. 9. The relatively closed nature of the resulting curves further illustrates the presence of a low-dimensional attractor in the form of a two-dimensional torus composed of two limit cycles or periodic solutions with two frequencies. The presence of two different frequencies can be inferred by comparing the number of closed loops in each limit cycle. In particular, the single-loop projections Figs. 9a i and 9b i represent the passing of one blade in the rotor across one stator airfoil. The flow in the turbine was computed for more than 80 cycles. Only one cycle, however, was used for the POD analysis. This cycle is described by the phase-space projections in Figs. 9a i and 9b i. The limit cycles in Figs. 9a ii and 9b ii,

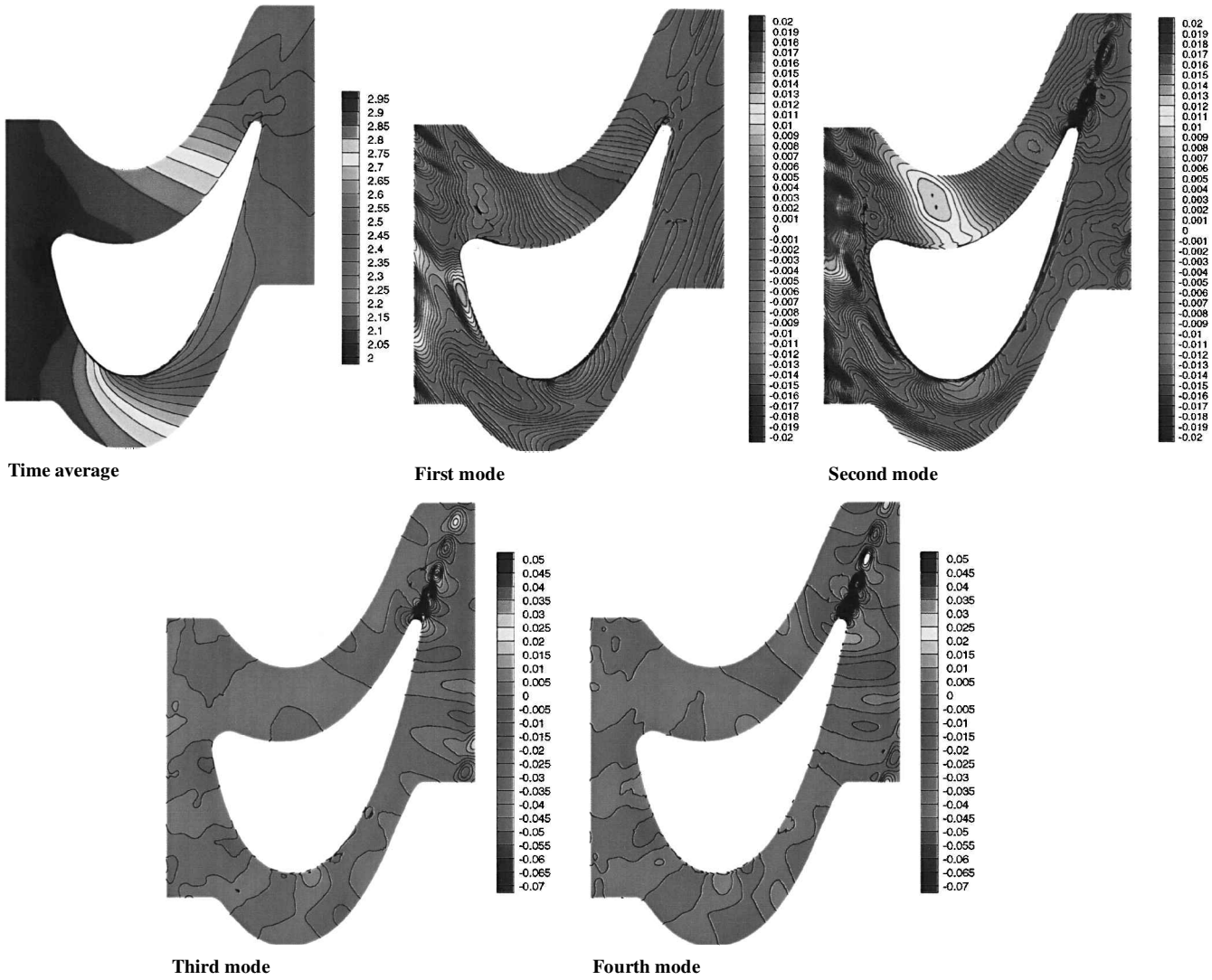

Fig. 6 Five most relevant POD modes for the state variable e on the rotor airfoil.

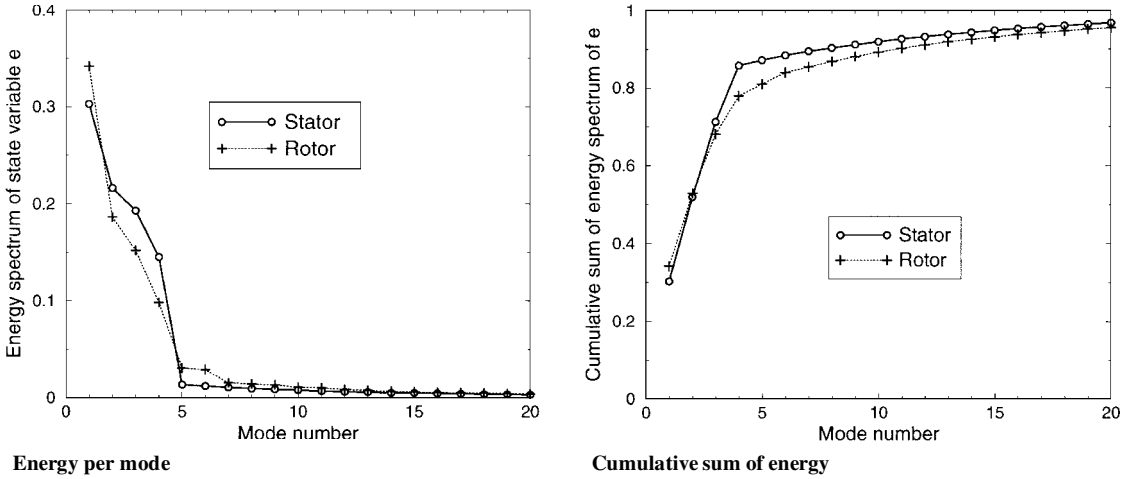

Fig. 7 POD energy spectrum in the decomposition of state variable e.

which contain approximately 10 loops, correspond to higher harmonics of the flow motion.

The POD reconstruction of energy in the stator and rotor rows at time $t = 0$ is shown in Figs. 10 and 11. By comparing these results with the original, full-model, spatiotemporal evolution of energy shown in Fig. 4, one can conclude that most of the details of the flow are captured by using 40 POD modes. This conclusion is also supported by the analysis of the shear stress variation on the rotor airfoil, shown in Fig. 12. Note that the stator flow is better captured than the rotor flow. This result is due to the flow on the rotor being more complicated, mainly due to the impact of the wakes coming from the stator.

The variation of the average, maximum, and minimum shear stresses on the rotor airfoil is shown in Fig. 12. The average shear stress is calculated over a cycle. The maximum shear stress shown in Fig. 12b represents the maximum values reached during a cycle

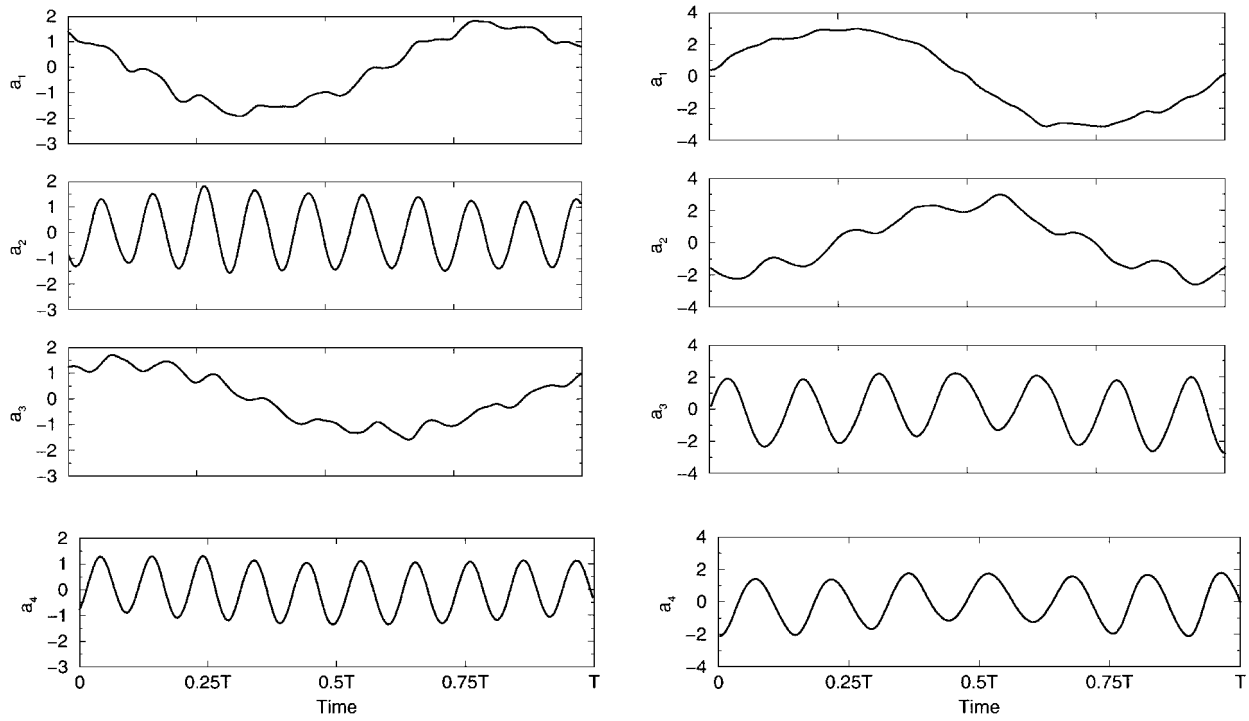

a) Stator b) Rotor

Fig. 8 Time series of POD amplitude coefficients in the decomposition of state variable *e*.

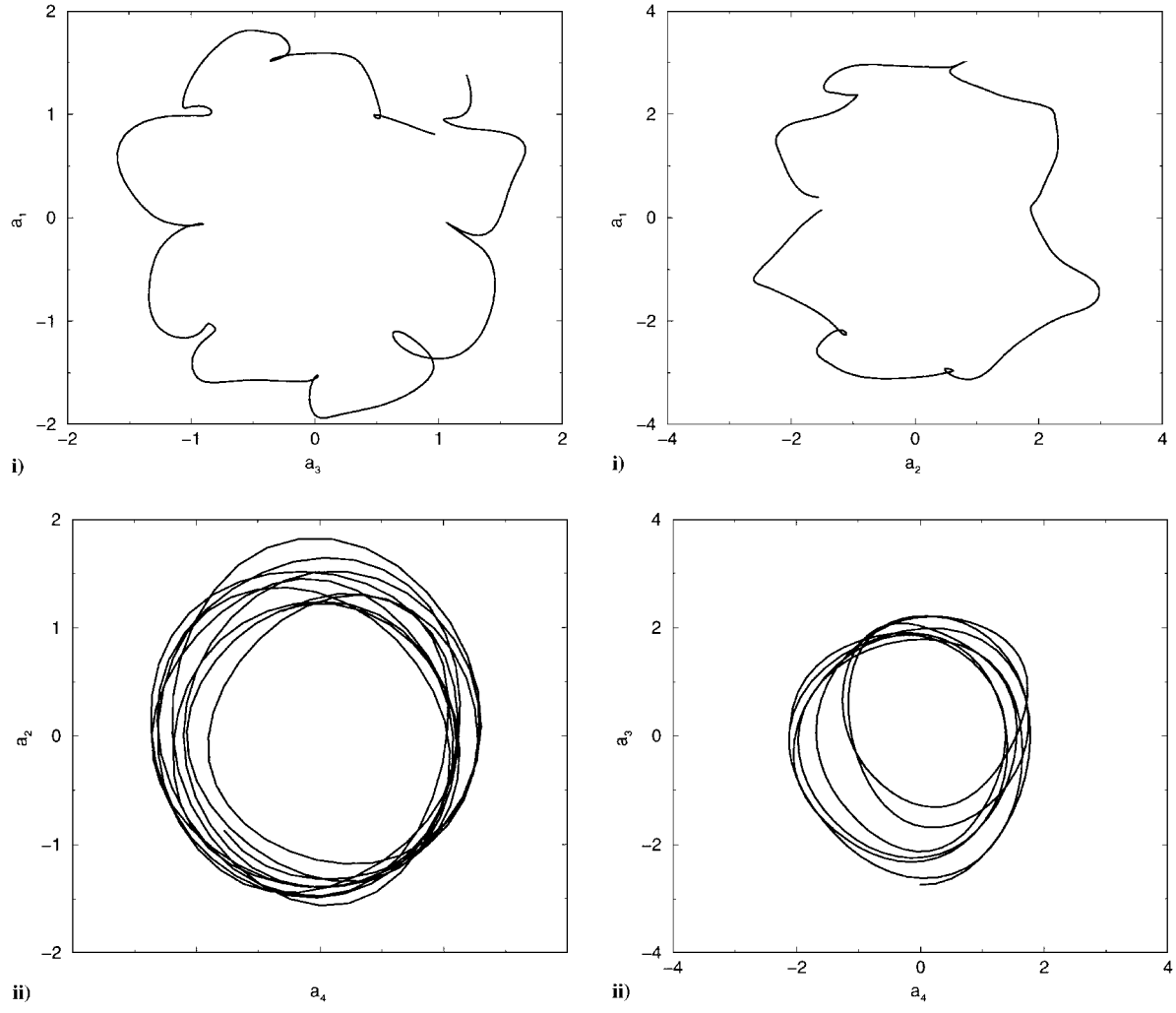

a) Stator b) Rotor

Fig. 9 Phase-space projections of the POD amplitude coefficients for state variable *e*.

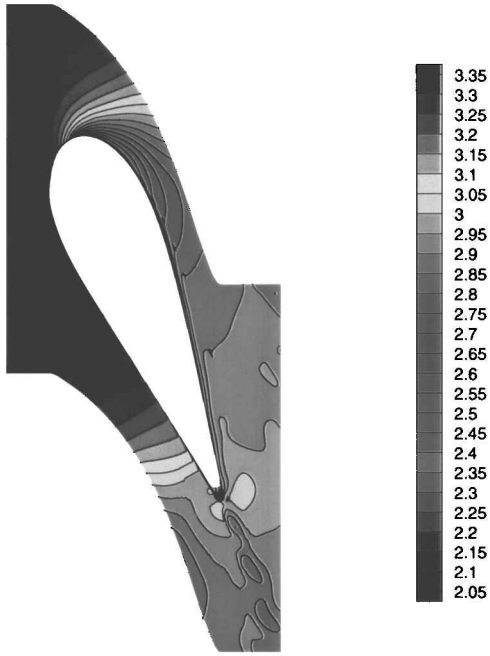

Fig. 10 POD reconstruction of state variable e on the stator at $t = 0$ using 40 modes.

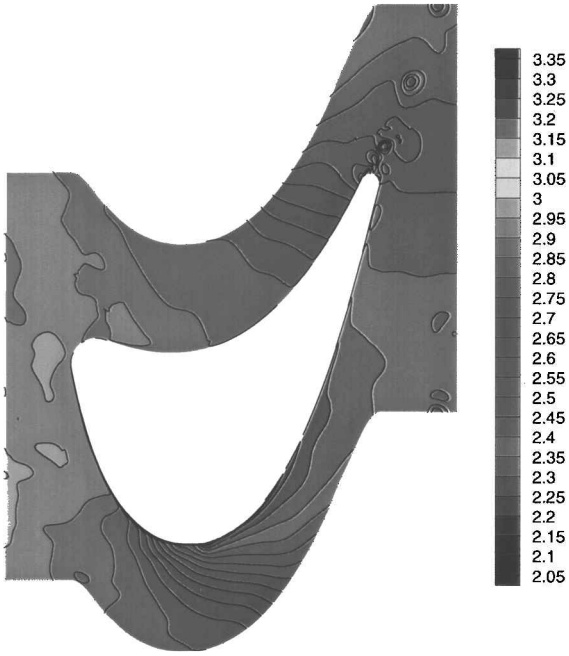

Fig. 11 POD reconstruction of state variable e on the rotor at $t = 0$ using 40 modes.

at any location on the airfoil, $\tau_i^{\max} = \max_{j \in [1,N]} \tau_i^j$, where N is the number of time steps in a cycle and i is the grid point index. Similarly, the minimum shear stress shown in Fig. 12c represents the minimum values reached during a cycle at any location on the airfoil. The shear stress values obtained using 10, 20, 30, and 40 POD modes are compared against the full-model (FM) solution, that is, the solution obtained by solving the Navier–Stokes equations. The largest differences between the FM solution and the POD reconstructed solution are shown in Table 3. Two values of the error are defined and calculated for the average, maximum, and minimum stresses: 1) a local error ϵ_ℓ and 2) a global error ϵ_g. The two errors are defined as

$$\epsilon_\ell = \max_{i \in [1,N_G]} \frac{\left|\tau_i - \tau_i^{\text{POD}}\right|}{\tau_{\max} - \tau_{\min}} \tag{14}$$

Table 3 Variation of the difference between the rotor shear stresses calculated using the full model solution and the POD reconstructed solution

Number of POD modes	Average		Maximum		Minimum	
	ϵ_g,%	ϵ_ℓ,%	ϵ_g,%	ϵ_ℓ,%	ϵ_g,%	ϵ_ℓ,%
10	0.105	1.52	0.26	4.48	0.41	6.73
20	0.105	1.52	0.19	3.80	0.26	5.12
30	0.105	1.52	0.20	3.92	0.25	6.32
40	0.105	1.52	0.20	3.04	0.25	6.02

$$\epsilon_g = \frac{1}{N_G} \sum_{i=1}^{N_G} \frac{\left|\tau_i - \tau_i^{\text{POD}}\right|}{\tau_{\max} - \tau_{\min}} \tag{15}$$

where N_G is the number of grid points on the airfoil, τ_i is the shear stress at grid point i calculated using the full model solution, and τ_i^{POD} is the shear stress at grid point i calculated using the POD reconstructed solution. Here, $\tau_{\max}$ and $\tau_{\min}$ are defined as $\tau_{\max} = \max_{i \in [1,N_G]} \tau_i$ and $\tau_{\min} = \min_{i \in [1,N_G]} \tau_i$. The results shown in Table 3 indicate that the average shear stress is captured properly by using only 10 POD modes, the local and global errors being approximately 1.5 and 0.1%, respectively. More POD modes are necessary to capture the maximum and minimum shear stresses. By the use of 40 POD modes, the local and global errors of the minimum shear stresses are approximately 6 and 0.2%, respectively. The local and global errors of the maximum shear stresses are approximately 3 and 0.2%, respectively.

Another way to visualize the differences between the FM solution and the POD reconstructed solution is to plot the differences between the two solutions. Figure 13 shows the difference between the FM solution of the energy e on the stator and its 40 mode POD reconstruction. The differences between the two solutions vary between -0.0141 and 0.0123. Consequently, the error varies at most between -0.61 and 0.53%. The largest errors occur in the region that is facing the downstream row, and they are concentrated in the wake region.

Figure 14 shows the difference between the FM solution of the energy e on the rotor and its 40 mode POD reconstruction. The differences between the two solutions vary between -0.1406 and 0.0825. Consequently, the error varies at most between -6.75 and 3.95%. As opposed to the stator, where the errors were concentrated downstream of the airfoil, the errors are more evenly spread on the rotor. The error level in the upstream region of the rotor airfoil varies as a function of the relative position between the rotor and the stator. The error level in the wake is rather constant, being less affected by the relative position between the rotor and the stator. The largest level of the errors in the region upstream of the rotor airfoil corresponds to time $t = 0$, when the wakes of the stator are convected through the middle of the passage between the rotor blades. The largest errors in the rotor are concentrated in the wake.

Figure 15 shows the variation of the differences between the FM solution and its POD reconstruction, as a function of the number of POD modes. The minimum and maximum values of the differences between the FM solution and its POD reconstruction are shown in Table 4. As expected, the larger the number of POD modes, the smaller the difference between the FM solution and its POD reconstruction is. One exception is noticed on the stator, where the error corresponding to the 40-mode reconstruction is larger than the error corresponding to the 30-mode reconstruction. Recall, however, that this error corresponds to time $t = 0$. Further analysis shows that the error varies in time in a nearly sinusoidal manner. The average value of the error corresponding to the 40-mode reconstruction is smaller than the average value of the error corresponding to the 30-mode reconstruction. The sum of the amplitudes of the 40- and 30-mode reconstruction errors is larger than the difference between the averaged values of the 40- and 30-mode errors. Consequently, instantaneous values of the 40-mode reconstruction error can be larger than the values of the 30-mode reconstruction error. Figure 16 compares 40- and 10-mode reconstruction.

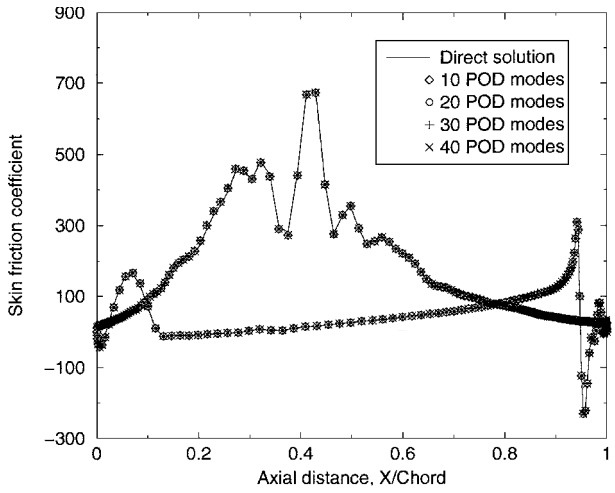

a) Average values

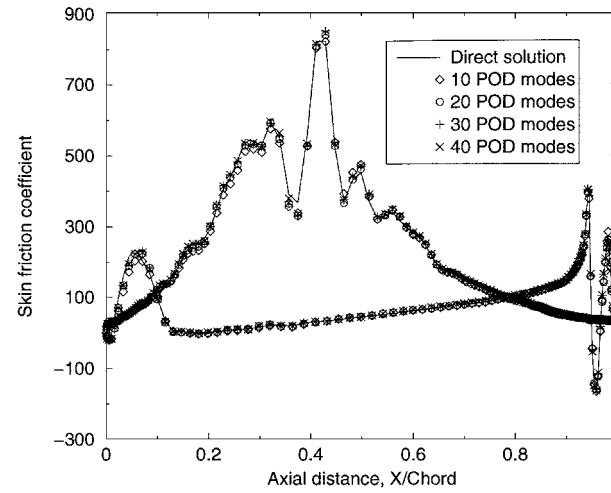

b) Maximum values

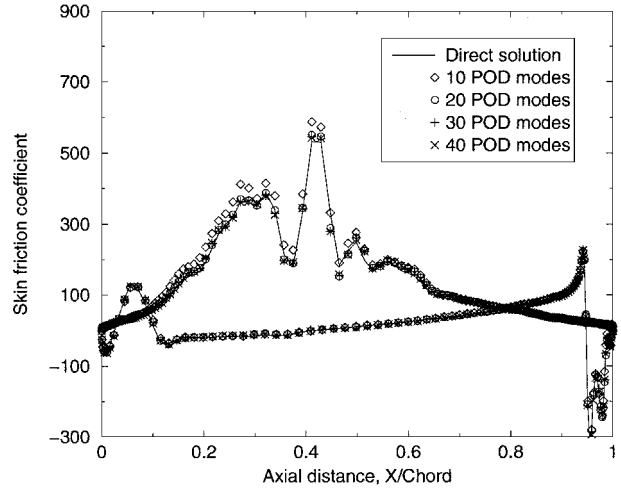

c) Minimum values

Fig. 12 Skin-friction variation on the rotor airfoil.

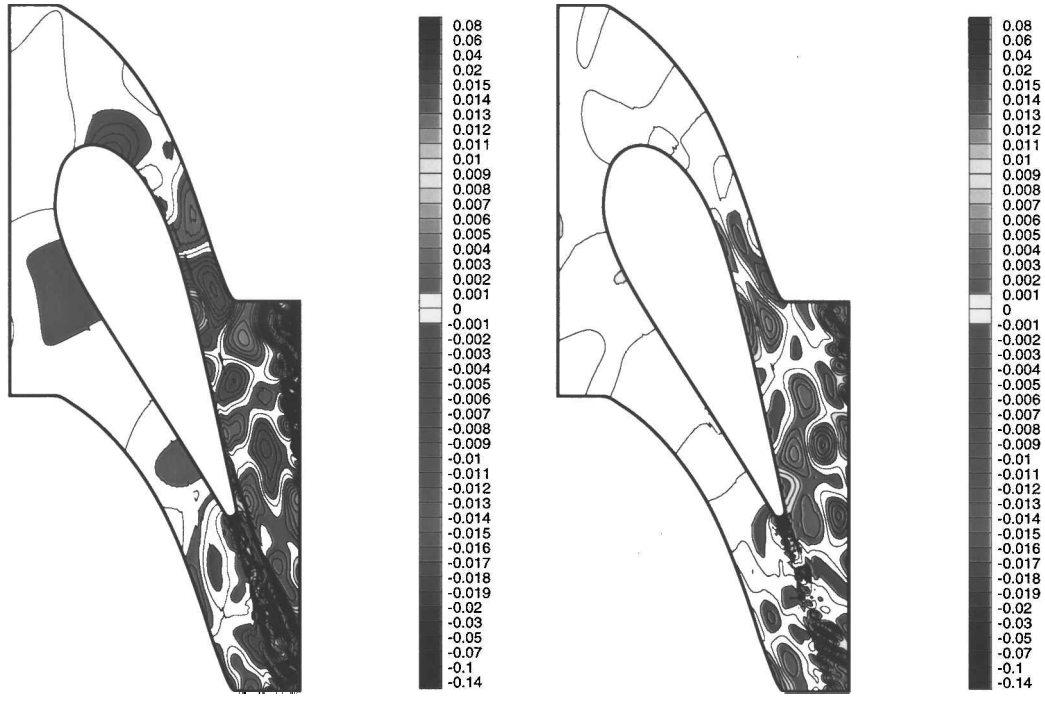

$t = 0$ $t = 0.5T$

Fig. 13 Difference between the simulated solution of the variable e on the stator and its 40 mode POD reconstruction.

Table 4 Variation of the difference between the full model solution of energy at time $t = 0$ and its reconstruction, as a function of the number of POD modes

Number of POD modes	Stator				Rotor			
	Minimum	(%)	Maximum	(%)	Minimum	(%)	Maximum	(%)
10	−0.0245	(−1.06)	0.03124	(1.36)	−0.1406	(−6.73)	0.0825	(3.95)
20	−0.0151	(−0.66)	0.01772	(0.77)	−0.0854	(−4.09)	0.0760	(3.64)
30	−0.0128	(−0.56)	0.01255	(0.54)	−0.0604	(−2.89)	0.0505	(2.42)
40	−0.0141	(−0.61)	0.01227	(0.53)	−0.0324	(−1.55)	0.0369	(1.76)

$t = 0$ $t = 0.5T$

Fig. 14 Difference between the simulated solution of the variable e on the rotor and its 40 mode POD reconstruction.

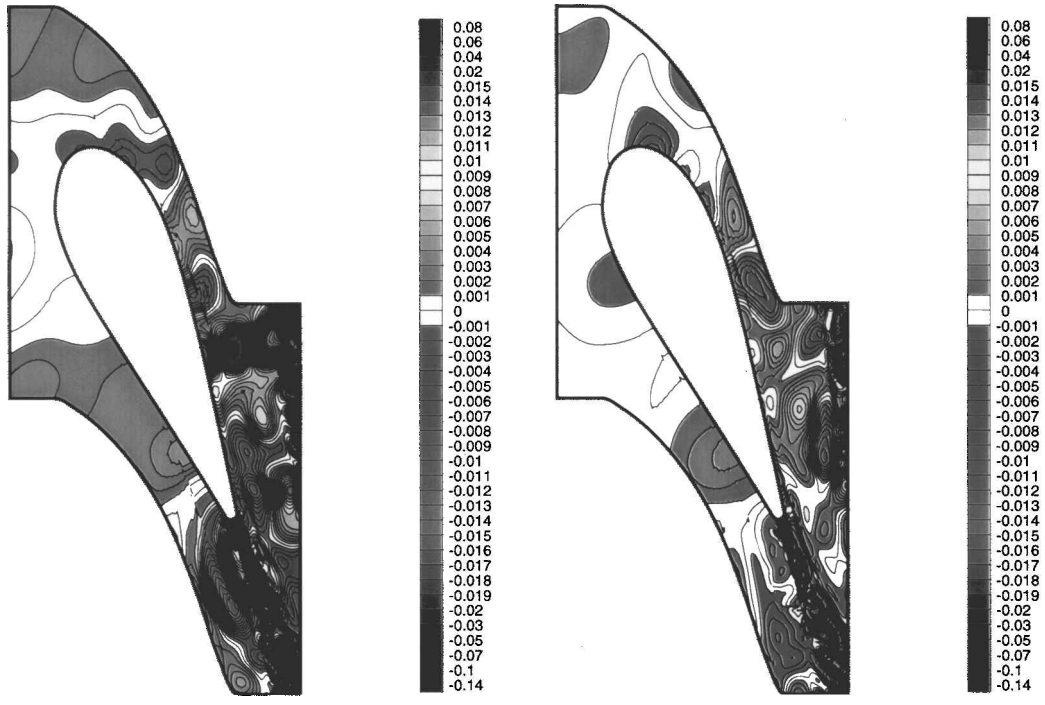

10 POD modes 40 POD modes

Fig. 15 Difference between the simulated solution of the variable e on the stator at time $t = 0$ and its POD reconstruction.

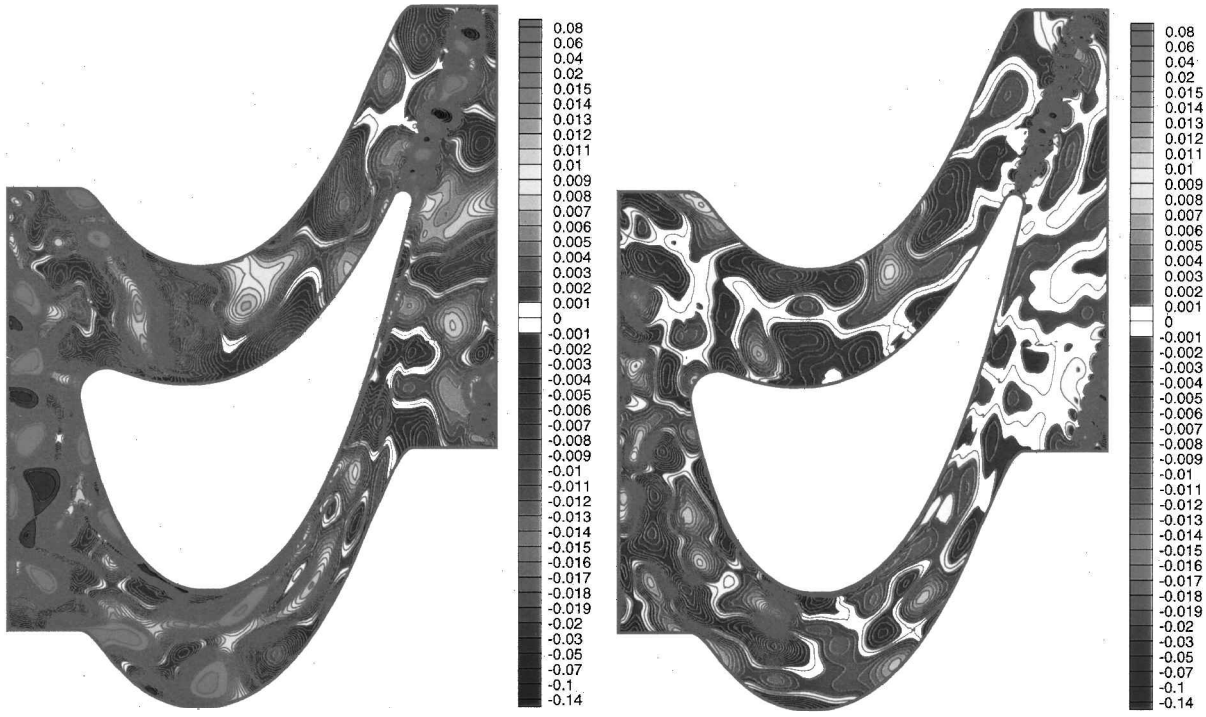

10 POD modes **40 POD modes**

Fig. 16 Difference between the simulated solution of the variable e on the rotor at time $t = 0$ and its POD reconstruction.

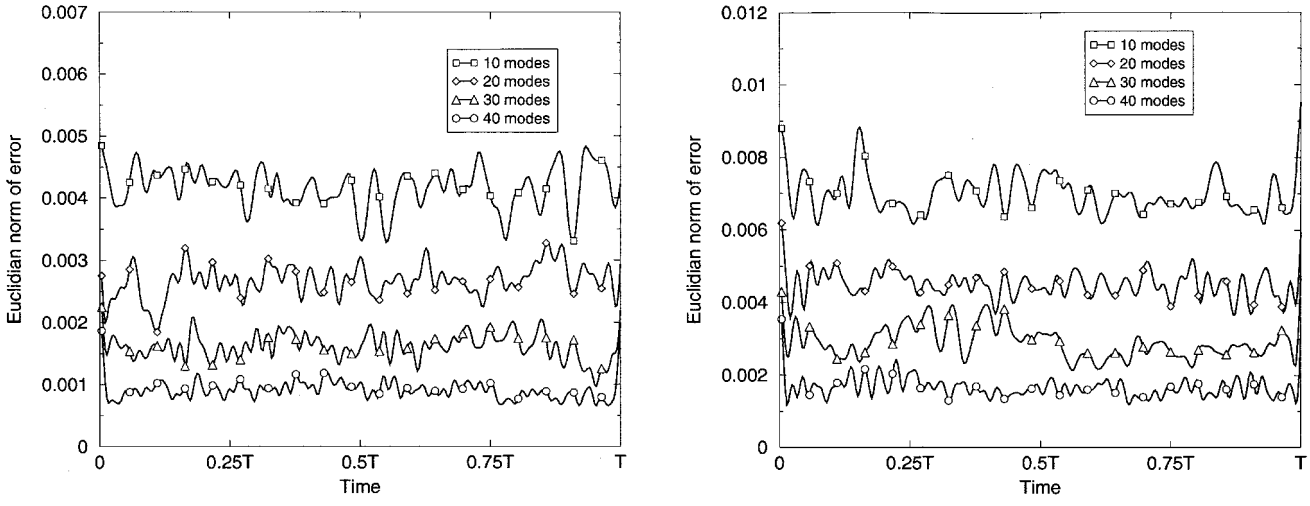

Stator **Rotor**

Fig. 17 Error variation of the POD reconstruction of variable e as a function of the number of POD modes and time.

Figure 17 shows the mean Euclidean norm of the difference between the FM solution of the energy e and its POD reconstruction,

$$\epsilon = \sqrt{\sum_{i=1}^{N_G} \frac{(e_{\mathrm{FM}} - e_{\mathrm{POD}})}{N_G}}$$

Here, N_G denotes the total number of grid points. Note that, in Fig. 17, the ordinate scale of the rotor is twice the stator scale. For both the stator and the rotor, the mean Euclidean norm of the error decreases as the number of POD modes increases. The mean Euclidean norm of the error on the rotor is approximately two times larger than that on the stator, due to a more complex flow interaction, caused mainly by the stator wakes.

POD of Density

As in the case of state variable e, most of the energy spectrum of density ρ is captured by the first four modes, as shown in Fig. 18a. The relative energy E_1 captured by the first mode is approximately 27% for the stator and 32% for the rotor. The relative energy E_5 captured by the fifth mode is less than 2% for both the stator and the rotor.

The time variation and the phase-space projections of the POD amplitude coefficients of density ρ are similar to those of the state variable e. For brevity, herein, only the error variation ϵ of the POD reconstruction is presented in Fig. 19. Note that the error ϵ of density is approximately three times smaller than the error ϵ of energy e, shown in Fig. 17.

This result suggests that if the variation of energy e is properly captured by N POD modes, then the variation of state variable ρ can

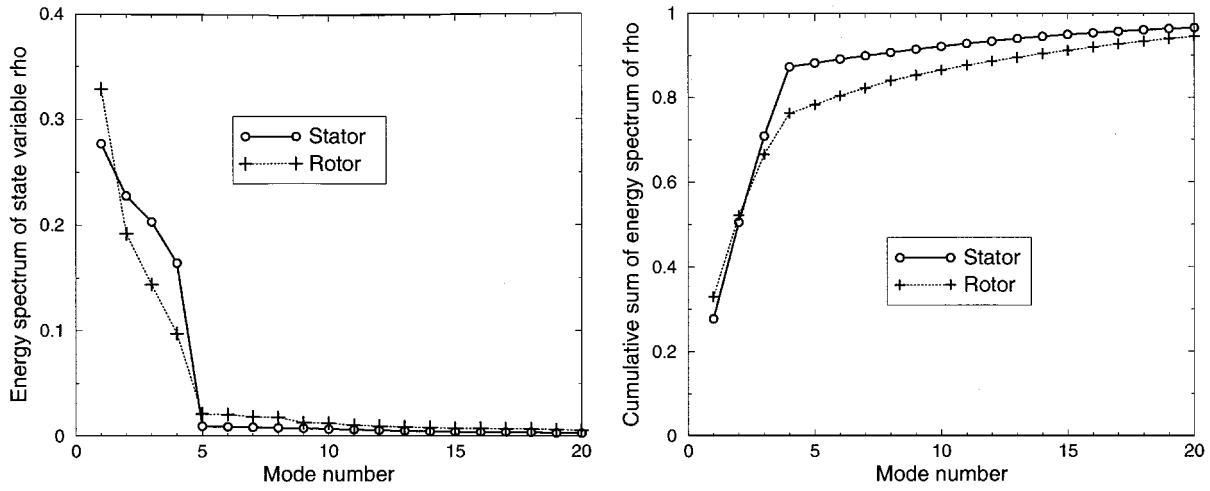

a) Energy per mode b) Cumulative sum of energy

Fig. 18 POD energy spectrum in the decomposition of state variable ρ.

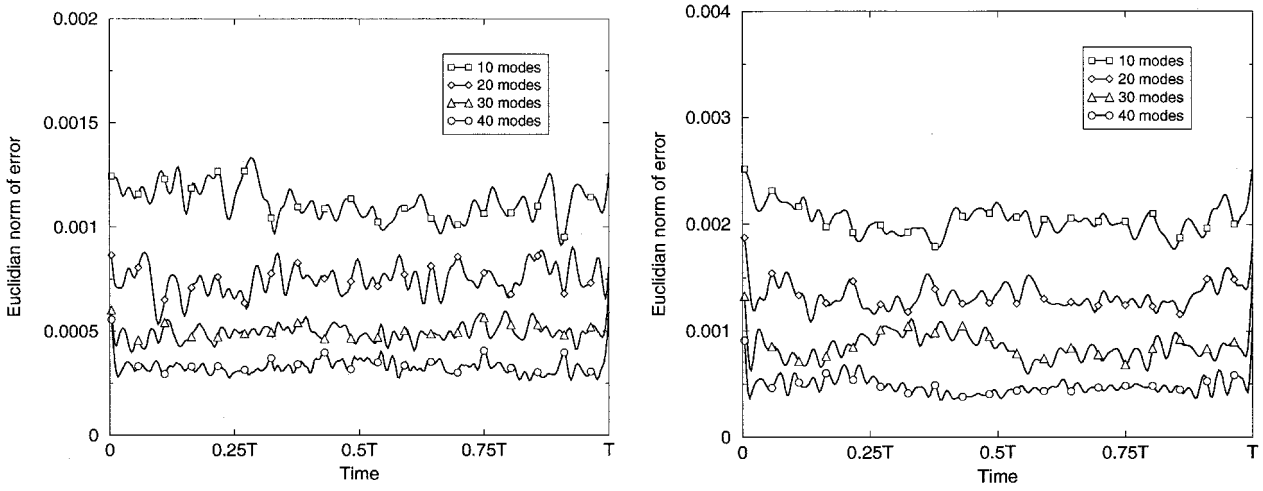

Stator Rotor

Fig. 19 Error variation of the POD reconstruction of variable ρ as a function of the number of POD modes and time.

also be captured by N or less POD modes. This conclusion is also valid for the state variables ρu and ρv, but, for brevity, the results corresponding to these two variables were not included.

Conclusions

Numerical simulations of rotor–stator interaction in a one-stage turbine were carried out to investigate the complex flow dynamics and to explore the validity of a reduced-order model based on the POD. The flow in the turbine was modeled by the Reynolds-averaged Navier–Stokes equations. The governing equations were written in the strong conservation form and solved using a fully implicit, finite difference approximation. By the use of the POD, the spatial dominant features were identified and separated from the spatiotemporal dynamics of the rotor–stator interaction. The numerical results indicate that 40 modes capture more than 99% of the energy spectrum of the state variables used to model the turbine flow. Phase-space plots further indicate the existence of low-dimensional dynamics, which supports the validity of a reduced-order model for turbine rotor–stator interaction. Projecting the governing equations onto the POD modes, as is commonly done in the Galerkin method, can lead to the desired reduced-order model. Such task is reserved for future work.

Acknowledgments

This work has been funded by the Department of Energy through Grant DE-FC26-00NT40903. We would like to thank Thomas O'Brien and John Rockey of the National Energy Technology Laboratory for their guidance and support. The work of the first author has also been supported by the Texas Advanced Research Program under Grant 000512-0116-1999and by Siemens Westinghouse Power Corporation. We would like to thank Thomas Lippert of Siemens Westinghouse Power Corporation for his guidance and support.

References

[1]Gundy-Burlet, K. L., and Dorney, D. J., "Three-Dimensional Simulations of Hot Streak Clocking in a 1-1/2 Stage Turbine," *International Journal of Turbo and Jet Engines*, Vol. 14, No. 3, 1997, pp. 133–144.

[2]Eulitz, F., Engel, K., and Gebbing, H., "Numerical Investigation of the Clocking Effects in a Multistage Turbine," American Society of Mechanical Engineers, ASME Paper 96-GT-26, June 1996.

[3]Cizmas, P. G. A., and Subramanya, R., "Parallel Computation of Rotor–Stator Interaction," *The Eighth International Symposium on Unsteady Aerodynamics and Aeroelasticity of Turbomachines*, edited by T. H. Fransson, Kluwer Academic Publishers, Dordrecht, Boston, London, 1997, pp. 633–643.

[4]Cizmas, P. G. A., and Dorney, D. J., "Parallel Computation of Turbine Blade Clocking," *International Journal of Turbo and Jet Engines*, Vol. 16, No. 1, 1999, pp. 49–60.

[5]Yao, J., Jameson, A., Alonso, J. J., and Liu, F., "Development and Validation of a Massively Parallel Flow Solver for Turbomachinery Flows," *Journal of Propulsion and Power*, Vol. 17, No. 3, 2001, pp. 659–668.

[6]Neurnberger, D., Eulitz, F., Schmitt, S., and Zachcial, A., "Recent Progress in the Numerical Simulation of Unsteady Viscous Multistage Turbomachinery Flow," ISABE, ISABE-2001-1081, Sept. 2001.

[7]Mahajan, A. J., Dowell, E. H., and Bliss, D. B., "Eigenvalue Calculation Procedure for Euler/Navier–Stokes Solvers with Application to Flows over Airfoils," *Journal of Computational Physics*, Vol. 97, No. 2, 1991, pp. 398–413.

[8]Mahajan, A. J., Dowell, E. H., and Bliss, D. B., "Role of Artificial Viscosity in Euler and Navier–Stokes Solvers," *AIAA Journal*, Vol. 29, No. 4, 1991, pp. 555–569.

[9]Florea, R., and Hall, K. C., "Reduced Order Modeling of Unsteady Flows About Airfoils," *Aeroelasticity and Fluid Structure Interaction Problems, ASME International Mechanical Engineering Congress and Exposition*, American Society of Mechanical Engineers, New York, 1994, pp. 49–68.

[10]Hall, K. C., Florea, R., and Lanzkron, P. J., "A Reduced Order Model of Unsteady Flows in Turbomachinery," *Journal of Turbomachinery*, Vol. 117, No. 3, 1995, pp. 375–383.

[11]Hall, K. C., "Eigenanalysis of Unsteady Flows About Airfoils, Cascades, and Wings," *AIAA Journal*, Vol. 32, No. 12, 1994, pp. 2426–2432.

[12]Florea, R., Hall, K. C., and Cizmas, P. G. A., "Reduced-Order Modeling of Unsteady Viscous Flow in a Compressor Cascade," *AIAA Journal*, Vol. 36, No. 6, 1998, pp. 1039–1048.

[13]Florea, R., Hall, K. C., and Cizmas, P. G. A., "Eigenmode Analysis of Unsteady Viscous Flows in Turbomachinery Cascades," *Proceedings of the Eighth International Symposium on Unsteady Aerodynamics and Aeroelasticity of Turbomachines*, edited by T. H. Fransson, Kluwer Academic Publishers, Dordrecht, Boston, London, 1997, pp. 767–782.

[14]Romanowski, M. C., "Using Fluid Eigenmodes to Develop Euler Based Reduced Order Unsteady Aerodynamic and Aeroelastic Models," Ph.D. Dissertation, Dept. of Mechanical Engineering and Materials Science, Duke Univ., Durham, NC, May 1995.

[15]Lucia, D. J., Beran, P. S., and King, P. I., "Reduced Order Modeling of an Elastic Panel in Transonic Flow," *Journal of Aircraft*, 43rd AIAA/ASME/ASCE/AHS Structures, Structural Dynamics, and Materials Conference, AIAA Paper 2002-1594, Denver, CO, April 2002.

[16]Rai, M. M., "Navier–Stokes Simulation of Rotor–Stator Interaction Using Patched and Overlaid Grids," *Journal of Propulsion and Power*, Vol. 3, 1987, pp. 387–396.

[17]Cizmas, P. G. A., and Subramanya, R., "A Parallel Algorithm for Simulation of Unsteady Flows in Multistage Turbomachinery, *International Journal of Turbo and Jet Engines*, Vol. 18, No. 2, 2001, pp. 117–131.

[18]Karhunen, K., "Zur Spektraltheorie Stochasticher," *Annales Academiae Scientiarum Fennicae Series A1*, Vol. 1, 1946, p. 34.

[19]Loeve, M., *Probability Theory*, Van Nostrand, New York, 1955, pp. 77–130.

[20]Berkooz, G., Holmes, P., and Lumley, J. L., "The Proper Orthogonal Decomposition in the Analysis of Turbulent Flows," *Annual Review of Fluid Mechanics*, Vol. 25, 1993, pp. 539–575.

[21]Holmes, P., Lumley, J., and Berkooz, G., *Turbulence, Coherent Structures, Dynamical Systems and Symmetry*, Cambridge Univ. Press, Cambridge, England, U.K., 1996, pp. 86–144.

[22]Lumley, J. L., "The Structure of Inhomogeneous Turbulent Flows," *Atmospheric Turbulence and Radio Wave Propagation*, edited by A. Yaglom and V. Tatarski, Nauka, Mosco, 1967, pp. 167–178.

[23]Graham, M. D., Lane, S. L., and Luss, D., "Proper Orthogonal Decomposition Analysis of Spatiotemporal Temperature Patterns," *Journal of Physical Chemistry*, Vol. 97, No. 4, 1993, pp. 889–894.

[24]Preisendorfer, R. W., *Principal Component Analysis in Meteorology and Oceanography*, Elsevier, Amsterdam, 1988, pp. 11–120.

[25]Pratt, K. W., *Digital Image Processing*, 2nd ed., Wiley, New York, 1991.

[26]Pettit, C. L., and Beran, P. S., "Reduced-Order Modeling for Flutter Prediction," *41st AIAA/ASCE/AHS/ASC Structural, Structural Dynamics and Materials Conference*, AIAA Paper 2000-1446, April 2000.

[27]Sirovich, L., "Turbulence and the Dynamics of Coherent Structures," *Quarterly of Applied Mathematics*, Vol. 45, No. 3, 1987, pp. 561–590.

[28]Stewart, D. E., and Leyk, Z., "Meschach: Matrix Computations in C," *CMA Proceedings No. 32*, Australian National Univ., Canberra, Australia, ACT, 1994, pp. 4–150.

[29]Cizmas, P. G. A., "Transition and Blade Count Influence on Steam Turbine Clocking," Technical Rept. 56960, Texas Engineering Experiment Station, College Station, TX, Jan. 1999.